高等学校化学学报
CHEMICAL JOURNAL OF CHINESE UNIVERSITIES
研究论文

# 原位激活型近红外二区聚集诱导发光探针应用于肿瘤中过氧化氢的高灵敏成像

朱高桦[1#]，舒　菊[1#]，耿江涛[1#]，马夫龙[1]，熊玲红[2]，何学文[1]
（1. 苏州大学材料与化学化工学部，仿生界面材料科学国家重点实验室，
苏州市健康化学与分子诊断重点实验室，苏州 215123；
2. 苏州大学苏州医学院公共卫生学院，苏州 215123）

**摘要**　原位高灵敏精准肿瘤传感技术对于癌症的早期诊断与治疗具有重大意义. 其中，基于肿瘤标志物的荧光传感凭借其灵敏度高、操作简便及原位实时检测等优势受到广泛关注. 实现高质量的肿瘤荧光成像从根本上依赖于高性能的发光探针，而开发具有优异组织穿透深度和超高响应灵敏度的近红外二区(NIR-II)荧光探针为此提供了一条极具前景的解决路径. 本文报道了一种具有聚集诱导发光特性的近红外二区荧光探针4,4′-{6,7-二(噻吩-2-基)-[1,2,5]噻二唑并[3,4-g]喹喔啉-4,9-二基}双{*N*,*N*-二甲基-*N*-[4-(4,4,5,5-四甲基-1,3,2-二氧杂硼杂环戊烷-2-基)苄基]苯胺鎓}(TQT-Bpin)，其能够特异性响应肿瘤内过表达的过氧化氢，从而原位激活近红外二区荧光发射. 该探针展现出卓越的灵敏度与特异性，能够实现对肿瘤区域过氧化氢的实时、原位、响应性传感与成像，并表现出超大的斯托克斯位移(320 nm)、良好的选择性(检出限低至3.6 μmol/L)及优异的稳定性. 这种集深度组织穿透、高灵敏度及原位响应能力于一体的近红外二区探针为肿瘤早期检测提供了新策略.

**关键词**　荧光探针；近红外二区；聚集诱导发光；过氧化氢；原位激活
**中图分类号**　O631　　**文献标志码**　A　　doi：10.7503/cjcu20260058

# *In situ* Activating NIR-II AIE Probe for Highly Sensitive Hydrogen Peroxide Imaging in Tumor

ZHU Gaohua[1#], SHU Ju[1#], GENG Jiangtao[1#], MA Fulong[1*], XIONG Linghong[2*], HE Xuewen[1*]
(*1. State Key Laboratory of Bioinspired Interfacial Materials Science, the Key Lab of Health Chemistry and Molecular Diagnosis of Suzhou, College of Chemistry, Chemical Engineering and Materials Science, Soochow University, Suzhou* 215123, *China*;
*2. School of Public Health, Suzhou Medical College of Soochow University, Suzhou* 215123, *China*)

**Abstract**　*In situ* highly sensitive and accurate tumor sensing is of great significance for early cancer diagnosis and treatment. Fluorescence sensing of tumor biomarkers has attracted considerable attention due to its advantages of high sensitivity, operational simplicity, and capability for real-time *in situ* detection. Achieving high-quality tumor fluorescence imaging fundamentally depends on high-performance luminescent probes, and developing near-infrared-II (NIR-II) fluorescent probes with excellent tissue penetration depth and ultra-high response sensitivity provides a highly promising solution path for this. Herein, we report a NIR-II fluorescent probe,

收稿日期：2026-02-01. 网络首发日期：2026-04-09.
联系人简介：何学文，男，博士，教授，主要从事新型荧光探针和生化分析方面的研究. E-mail：xheao@suda.edu.cn
熊玲红，女，博士，副教授，主要从事病原微生物检测与杀灭方面的研究. E-mail：xionglinghong@suda.edu.cn
马夫龙，男，博士，副教授，主要从事近红外二区荧光探针方面的研究. E-mail：flma@suda.edu.cn
基金项目：国家自然科学基金(批准号：22274106)和苏州大学启动经费资助.
Supported by the National Natural Science Foundation of China(No.22274106) and the Startup Funds from Soochow University, China.
# 共同第一作者.

4,4′-{6,7-di(thiophen-2-yl)-[1,2,5]thiadiazolo[3,4-g]quinoxaline-4,9-diyl} bis{*N*,*N*-dimethyl-*N*-[4-(4,4,5,5-tetramethyl-1,3,2-dioxaborolan-2-yl)benzyl]benzenaminium}(TQT-Bpin), featuring aggregation-induced emission (AIE) characteristics. This probe can specifically respond to the hydrogen peroxide overexpressed in the tumor region, thereby *in situ* activating NIR-II fluorescence emission. It exhibits exceptional sensitivity and specificity, enabling real-time and responsive sensing and imaging of hydrogen peroxide in tumor areas, with advantages including an ultra-large Stokes shift (320 nm), excellent selectivity (limit of detection down to 3.6 μmol/L), and superior stability. Such an NIR-II probe, which integrates deep tissue penetration, high sensitivity, and *in situ* responsiveness, provides a novel strategy for early diagnosis of tumors.

**Keywords** Fluorescent probe; NIR-II region; Aggregation-induced emission; Hydrogen peroxide; *In situ* activating

## 1 Introduction

The high invasiveness and mortality rates of malignant tumors pose a severe threat to human health, making high-precision *in situ* tumor detection technology of critical importance for early diagnosis and treatment[1,2]. Conventional imaging modalities such as computer tomography (CT), magnetic resonance imaging (MRI), and positron emission tomography (PET) have been widely used in tumor detection, yet limitations remain: CT and MRI exhibit limited sensitivity for small lesions; PET/CT offers higher sensitivity but faces radioactive risk. Recently, fluorescence imaging has emerged as a promising approach for *in situ* visualization of tumors, owing to its high sensitivity, excellent spatiotemporal resolution, operational simplicity, and non-radioactivity[3—5]. The development of fluorescent probes that can specifically recognize and respond to the intratumoral biomarkers is of paramount importance[6—12]. Hydrogen peroxide($H_2O_2$), as an important reactive oxygen species, plays a key role in tumorigenesis and progression. Compared with normal tissues, tumor cells exhibit consistently and significantly elevated levels of $H_2O_2$ due to metabolic abnormalities, which makes $H_2O_2$ an ideal target for tumor identification[13]. Accordingly, designing and constructing "turn-on" fluorescent probes with high selectivity and responsiveness to $H_2O_2$ can convert abnormal chemical signals into sensitive optical signals, thereby providing new opportunities for *in vivo*, real-time detection and imaging of tumor regions.

Recently, numerous $H_2O_2$-responsive fluorescent probes based on fluorophores such as naphthalimide and boron dipyrromethene (BODIPY) have been reported[14—17]. However, the optical performance of these conventional probes is constrained by inherent limitations that restrict their application in complex physiological media. Their emission is confined to the visible(<650 nm) and first near-infrared(NIR-I, 650—900 nm) windows, which significantly overlap with tissue autofluorescence, posing challenges of high background interference and low signal-to-noise ratio. Furthermore, the excitation wavelengths of such probes are generally short, which not only limits their penetration depth but also accompanies potential photo-damage effects. The development of fluorescent probes emitting in the second near-infrared wavelength window (NIR-II, 900—1700 nm) offers an ideal solution for detecting $H_2O_2$ in biological systems[18,19]. Compared to short-wavelength fluorescence, NIR-II emission features have reduced absorption and scattering in tissues. This effectively minimizes autofluorescence while markedly improving both penetration depth and signal-to-noise ratio, thus enabling high-performance imaging[20,21]. Therefore, developing novel NIR-II fluorescent probes with deep penetration depth and high signal-to-noise ratio is of great significance for high-contrast *in situ* tumor sensing and imaging.

Extending the $\pi$-conjugation of molecular probes is an effective strategy to reduce the energy gap between ground and excited states, thereby achieving markedly red-shifted emission. However, this approach often increases molecular hydrophobicity, promoting aggregation *via* $\pi$-$\pi$ stacking in physiological environments

and ultimately leading to fluorescence quenching[22,23]. Such aggregation-caused quenching (ACQ) not only attenuates detection sensitivity but also can generate misleading signals. In contrast, aggregation-induced emission (AIE) materials typically feature highly twisted conformations that suppress non-radiative decay from molecular motion and prevent detrimental $\pi$-$\pi$ interactions[24—29]. Consequently, they retain high luminescence efficiency even in the aggregated state. Moreover, their distorted structures and AIE behavior contribute to large Stokes shifts and excellent photostability[30,31]. Therefore, developing fluorescent probes that integrate both NIR-II emission and AIE characteristics offers an ideal platform for sensitive detection, high-contrast imaging, and deep-tissue analysis of hydrogen peroxide.

Given the unique advantages of NIR-II fluorescence emission and AIE characteristics for high-contrast bioimaging, a novel activatable NIR-II AIE probe, 4,4′-{6,7-di(thiophen-2-yl)-[1,2,5]thiadiazolo[3,4-g]quinoxaline-4, 9-diyl} bis {*N*,*N*-dimethyl-*N*-[4-(4, 4, 5, 5-tetramethyl-1, 3, 2-dioxaborolan-2-yl) benzyl] benzenaminium} (TQT-Bpin), was designed and synthesized. This probe demonstrated not only excellent specificity for $H_2O_2$ recognition but also the capability for *in situ* activation within the tumor microenvironment. As shown in Scheme 1, the probe incorporated a twisted donor-acceptor (D-A) structured fluorophore, coupled with a phenylboronic acid pinacol ester group as the responsive unit. Due to the suppressed intramolecular charge transfer (ICT) effect, probe TQT-Bpin was almost non-emissive in the NIR-II region. Upon reaction with $H_2O_2$, cleavage of the phenylboronic acid pinacol ester moiety restored the ICT process, triggering strong fluorescence emission at 1004 nm. The probe demonstrated excellent sensitivity, with a limit of detection (LOD) of 3.6 μmol/L, and selectivity toward $H_2O_2$, along with a large Stokes shift (320 nm) and good stability. TQT-Bpin was successfully applied for *in situ* activation and high-sensitivity fluorescence imaging in mouse tumor models.

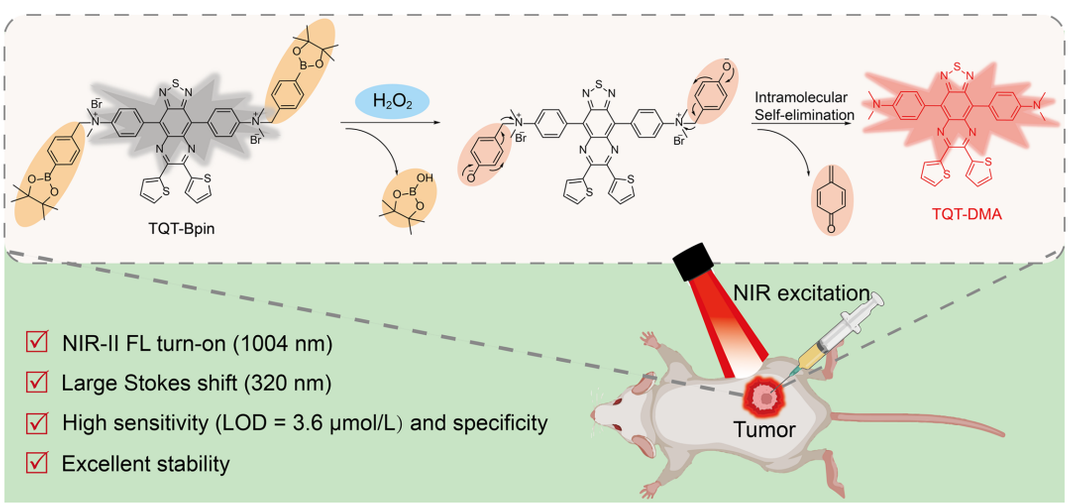


**Scheme 1 Schematic illustration of the response mechanism of TQT-Bpin to $H_2O_2$ and its advantages for tumor imaging**

## 2 Experimental

### 2.1 Materials and Measurements

*n*-Butyllithium (*n*-BuLi, 2.5 mol/L in hexane) and sodium nitrite ($NaNO_2$, purity 99%) were purchased from Energy Chemical; zinc powder (purity 99.99%) was purchased from Shanghai Aladdin Biochemical Technology Co., Ltd.; ammonium chloride ($NH_4Cl$, purity 99.5%), sodium nitrate ($NaNO_3$, purity 99.5%), sodium hydroxide (NaOH, A.R.), and glacial acetic acid (HAc, A.R.) were purchased from Sinopharm Chemical Reagent Co., Ltd.; [1,1′-bis(diphenylphosphino)ferrocene]dichloropalladium(II) [Pd(dppf)$Cl_2$],

4-bromomethylphenylboronic acid pinacol ester (purity 95%), and 4,7-dibromo-5,6-dinitrobenzothiadiazole (purity 97%) were purchased from Beijing Leyan Technology Co., Ltd.; dimethyl sulfoxide (DMSO, purity 99.5%) and hydrogen peroxide ($H_2O_2$, mass fraction 30%) were purchased from Suzhou Yonghua Chemical Co., Ltd.; methylene blue (MB, purity 95%), *tert*-butyl hydroperoxide (TBHP, purity 70%), and sodium hypochlorite (NaClO, mass fraction 6%—14%) were sourced from Shanghai Adamas Reagent Co., Ltd.; ferric chloride hexahydrate ($FeCl_3 \cdot 6H_2O$, purity 98%) was purchased from Alfa Aesar (China) Chemical Co., Ltd.; copper (II) chloride ($CuCl_2$, purity 99.99%) was purchased from Sigma-Aldrich (Shanghai) Trading Co., Ltd.; 4-bromo-*N*,*N*-dimethylaniline (purity 98%) and 2,2′-bithiophene-5,5′-dione (98%) were purchased from Shanghai Macklin Biochemical Co., Ltd.; tributyltin chloride (purity 97%) was purchased from Tokyo Chemical Industry Co., Ltd., Japan; phosphate-buffered saline (10×PBS) and fetal bovine serum (FBS) were sourced from Thermo Fisher Scientific (HyClone), America; try3-(4,5-dimethylthiazol-2-yl)-2,5-diphenyltetrazolium bromide (MTT, purity 97.5%), Sigma-Aldrich (Shanghai) Trading Co., Ltd. (America); ultrapure water (18.2 MΩ·cm) was purified using a Milli-Q Direct-8 water purification system (Millipore).

$^1H$ and $^{13}C$ nuclear magnetic resonance (NMR) spectra were recorded on a Bruker AVANCE NEO 300 MHz, a Bruker AVANCE NEO 400 MHz or a Bruker AVANCE NEO 600 MHz NMR spectroment. High-resolution mass spectra (HRMS) were performed using an electrospray ionization source on an Xevo G2-XS Tof mass spectrometer. Absorption spectra were recorded on an Agilent 8453 spectrophotometer. Fluorescence spectra and absolute fluorescence quantum yield were measured using an Edinburgh FLS1000 spectrofluorometer with an integrating sphere. The 808 nm laser was acquired from Ningbo Fengke Optoelectronics Co., Ltd. (FC-LPS-II). Dynamic light scattering (DLS) measurements were performed using a Zetasizer Nano ZS90 spectrometer (Malvern Panalytical Ltd., United Kimgdom) at a scattering angle of 90° with a helium-neon laser. Fluorescence imaging was conducted using a Series II 900/1700 small animal imaging system manufactured by Suzhou Yingrui Optics Technology Co., Ltd.

### 2.2 Synthetic Procedure

2.2.1 Synthesis of 4,4′-(5,6-dinitrobenzo[c][1,2,5]thiadiazole-4,7-diyl) bis (*N*, *N*-dimethylaniline) (compound **3**) Under $N_2$ atmosphere, 2000 mg (10.0 mmol) of 4-bromo-*N*,*N*-dimethylaniline (compound **1**) was dissolved in 15 mL of distilled THF. The solution was cooled to −78 ℃ in a dry-ice/ethyl acetate bath and stirred for 10 min. Then, 4.4 mL (11 mmol) of *n*-butyllithium solution was added dropwise, and the mixture was stirred at −78 ℃ for 1 h. Subsequently, 3900 mg (12 mmol) of tributyltin chloride was added dropwise, and stirring was continued at the same temperature for 30 min. The reaction mixture was then allowed to warm to room temperature and stirred for 12 h. After completion, the reaction was quenched by the addition of 3 mL methanol. The mixture was extracted three times with dichloromethane and water. The combined organic layers were dried over anhydrous magnesium sulfate and concentrated under reduced pressure. The residue was dried under vacuum to afford *N*,*N*-dimethyl-4-(tributylstannyl) aniline (compound **2**) as a pale-yellow oil (4102 mg), which was used directly without further purification.

Under $N_2$ atmosphere, a mixture of 4102 mg (10 mmol) of compound **2**, 1745 mg (4.54 mmol) of 4,7-dibromo-5,6-dinitrobenzo[c][1,2,5]thiadiazole, and 166 mg (0.23 mmol) of [1,1′-bis(diphenylphosphino)-ferrocene] dichloropalladium [$Pd(dppf)Cl_2$] was dissolved in 40 mL of distilled THF. The reaction mixture was stirred at 80 ℃ overnight. Upon completion of the reaction as monitored by thin-layer chromatography (TLC), the solvent was removed under reduced pressure using a rotary evaporator. The residue was then treated with *n*-hexane to precipitate the product. After brief sonication, the mixture was filtered to collect the crude solid. The solid was washed thoroughly with methanol and dried under vacuum to afford compound **3** as a purple solid (1846 mg) with a yield of 87.5%. $^1H$ NMR (400 MHz, DMSO-$d_6$), $\delta$: 7.42 (d, $J$=8.8 Hz,

4H), 6.87(d, *J*=8.9 Hz, 4H), 3.02(s, 12H).

2.2.2 Synthesis of 4,4′-(6,7-di(thiophen-2-yl)-[1,2,5]thiadiazolo[3,4-g]quinoxaline-4,9-diyl)bis(*N*,*N*-dimethylaniline)(TQT-DMA) 300 mg(0.646 mmol) of compound **3**, 2309 mg(35.53 mmol) of zinc powder, and 864 mg(6.15 mmol) of ammonium chloride were charged into a flask under a $N_2$ atmosphere. A mixed solvent of 30 mL of dichloromethane, 3 mL of methanol, and 0.4 mL of deionized water was added, and the resulting mixture was stirred at room temperature for 30 min. After TLC monitoring indicated completion of the reaction, the mixture was filtered, and the solid residue was washed with dichloromethane. The combined filtrate was sequentially washed with saturated aqueous $NaHCO_3$ solution and deionized water. The organic layer was dried over anhydrous magnesium sulfate and concentrated under reduced pressure. The residue was dried *in vacuo* to afford 255 mg of 4,7-bis[4-(dimethylamino)phenyl]benzo[c][1,2,5]thiadiazole-5,6-diamine (compound **4**) as a crude product, which was used in the next step without further purification.

Under $N_2$ atmosphere, 255 mg(0.630 mmol) of compound **4** was dissolved in 8 mL of acetic acid. With stirring, a solution of 144 mg(0.646 mmol) of 1,2-di(thiophen-2-yl)ethane-1,2-dione in 5 mL of acetic acid was added dropwise over 10 min. The reaction mixture was then heated to 80 ℃ and stirred for about 12 h. After TLC confirmed reaction completion, the mixture was cooled to room temperature and poured into a saturated aqueous $NaHCO_3$ solution. The resulting mixture was extracted with dichloromethane. The combined organic extracts were dried over anhydrous magnesium sulfate and concentrated under reduced pressure. After ultrasonic dispersion, the mixture was filtered to obtain the crude product. The solid was washed repeatedly with methanol and dried under vacuum to afford TQT-DMA as a green solid product (330 mg, 0.56 mmol) with a yield of 86.5%. $^1$H NMR(400 MHz, DMSO-$d_6$), $\delta$: 7.97—7.92(m, 4H), 7.89 (dd, *J*=5.0, 1.1 Hz, 2H), 7.43(dd, *J*=3.8, 1.1 Hz, 2H), 7.18(dd, *J*=5.0, 3.7 Hz, 2H), 7.01—6.96 (m, 4H), 3.12(s, 12H). $^{13}$C NMR(151 MHz, DMSO-$d_6$), $\delta$: 153.26, 150.56, 145.74, 142.21, 135.06, 134.54, 131.51, 130.62, 128.29, 127.53, 122.74, 111.45. HRMS(ESI$^+$), *m*/z calculated for $C_{32}H_{26}N_6S_3$ [M+H]$^+$: 591.1454; found: 591.1461.

2.2.3 Synthesis of TQT-Bpin 10 mg(0.017 mmol) of TQT-DMA and 101 mg(0.34 mmol) of 4-bromomethylphenylboronic acid pinacol ester were placed in a 4 mL reaction tube. 0.5 mL of DMF was added, and the reaction was stirred at room temperature for 48 h. Upon completion, the product was precipitated with diethyl ether, and the solvent was removed by centrifugation. Diethyl ether was added again, and the product was washed by ultrasonication, followed by centrifugation. The washing procedure was repeated three times. The solid was dried under vacuum to afford 15 mg(0.0127 mmol) of TQT-Bpin as a yellow solid with a yield of 74.5%. $^1$H NMR(300 MHz, DMSO-$d_6$), $\delta$: 8.12(s, 8H), 7.93(d, *J*=5.0 Hz, 2H), 7.63(d, *J*=7.6 Hz, 4H), 7.52(d, *J*=3.7 Hz, 2H), 7.26— 7.17(m, 6H), 5.23(s, 4H), 3.74(s, 12H), 1.27(s, 24H). $^{13}$C NMR (151 MHz, DMSO-$d_6$), $\delta$: 152.85, 147.42, 144.54, 142.00, 136.66, 135.75, 134.93, 134.31, 132.53, 132.32, 131.70, 131.59, 128.75, 127.42, 121.60, 84.52, 72.26, 53.52, 25.15. HRMS(ESI$^+$), *m*/z: calculated for $C_{58}H_{62}B_2N_6O_4S_3^{2+}$[M]$^{2+}$, 512.2085; found: 512.2090.

### 2.3 Characterization of Photophysical Properties

TQT-Bpin and TQT-DMA molecules were dissolved in DMSO to prepare stock solutions with a concentration of 1 mmol/L. The stock solutions were diluted to a molecular concentration of 50 μmol/L using PBS(10 mmol/L, pH=7.4), with a final volume of 100 μL, and then the ultraviolet-visible(UV-Vis) absorption spectra and fluorescence spectra were measured.

### 2.4 Response Performance of the Probe

2.4.1 Time-dependent experiment A mixture was prepared in PBS buffer with a total volume of 100 μL, containing final concentrations of 50 μmol/L TQT-Bpin and 100 μmol/L $H_2O_2$, and incubated at 37 ℃.

Absorption and emission spectra were recorded at designated time points.

2.4.2 $H_2O_2$ concentration-dependent experiment TQT-Bpin (50 μmol/L) was reacted with varying concentrations of $H_2O_2$ (0, 10, 20, 30, 50, 100, 200, 300, 500, 1000 μmol/L) in PBS buffer with a total volume of 100 μL at 37 ℃ for 1.5 h. All concentrations are final concentrations. The absorption and emission spectra were subsequently recorded.

2.4.3 Selectivity experiment Singlet oxygen was prepared by the following method: 5 μL of 1 mmol/L TQT-Bpin solution, 1 μL of 10 mmol/L MB solution, and 94 μL of PBS buffer were mixed, then irradiated with 660 nm light for 10 min, followed by incubation at 37 ℃ for 1.5 h. For other interfering species, 10 mmol/L stock solutions of TBHP, $NaNO_3$, $CuCl_2·2H_2O$, NaClO, $NaNO_2$, and $FeCl_3·6H_2O$ were prepared with pure water. For the reaction, 5 μL of TQT-Bpin (1 mmol/L), 1 μL of the interfering species stock solution, and 94 μL of PBS buffer were mixed and then incubated at 37 ℃ for 1.5 h. DLS measurement: TQT-Bpin (50 μmol/L) was reacted with $H_2O_2$ (100 μmol/L) in PBS buffer at 37 ℃ for 1.5 h, and the particle size was measured before and after the reaction with $H_2O_2$. All concentrations are final concentrations.

2.4.4 Stability experiment The stability of TQT-Bpin was assessed in PBS and cell lysate ($2\times10^4$ cells/mL). A 1 mmol/L stock solution was diluted to 50 μmol/L with a total volume of 100 μL in each medium. Absorption and emission spectra before and after response to $H_2O_2$ (100 μmol/L) were examined at 24, 48, and 120 h. Particle size of TQT-Bpin were examined at 24, 48, and 72 h.

2.4.5 Cytotoxicity assay 100 μL of aliquots of CT26 cells ($1.5\times10^4$ cells) were seeded into a 96-well plate. After 12 h incubation, the cell culture medium was removed, and 100 μL of cell culture medium containing 0, 5, 10, 25, 50, 75, or 100 μmol/L TQT-Bpin was added and incubated at 37 ℃ for 40 min. The medium was then replaced with normal culture medium and incubation continued at 37 ℃ for 12 h. After that, the medium was replaced with 100 μL of medium containing 0.5 mg/mL MTT and incubated at 37 ℃ for 2 h. The medium was then replaced with 100 μL of DMSO, and the plate was shaken to dissolve the formazan crystals. The absorbance of the supernatant at 570 nm was measured using a TECAN Infinite M200 PRO plate reader.

### 2.5 Establishment of Tumor Models

All animal experimental procedures were approved by the Animal Protection and Use Committee of Soochow University and complied with relevant ethical standards. Female BALB/c mice (3—8 weeks old) were purchased from Jiangsu GemPharmatech Co., Ltd. A suspension of $2\times10^6$ CT26 cells in 100 μL of PBS was subcutaneously injected into the right flank of the mice. Fluorescence imaging experiments were performed when the tumor volume reached approximately 100 $mm^3$.

### 2.6 Fluorescence Imaging of Tumor in Mice

TQT-Bpin was dissolved in DMSO to prepare a stock solution (10 mmol/L), then diluted with PBS to a final concentration of 50 μmol/L. Mice were anesthetized with isoflurane, and 100 μL of the probe solution was administered *via* intratumoral injection. Fluorescence imaging was performed using a NIR-II small animal imaging system, with an excitation wavelength of 808 nm, laser power of 2 W, and exposure time of 400 ms. Fluorescence images were acquired at 0, 5, 10, 30, 45, 60, and 120 min post-injection.

## 3 Results and Discussion

### 3.1 Design and Synthesis of Probe

Dimethylaniline (DMA) exhibits strong electron-donating ability, while 6, 7-bis (thiophen-2-yl)-[1,2,5]thiadiazolo[3,4-g]quinoxaline(TQT) demonstrates pronounced electron-withdrawing properties[32]. By coupling the two moieties, the fluorophore of TQT-DMA with a donor-acceptor (D-A) structure was constructed. This design promotes a pronounced intramolecular charge transfer (ICT) effect, which effectively

reduces the energy gap and ultimately leads to emission in the NIR-II region. To achieve highly selective and sensitive detection of $H_2O_2$, a pinacol phenylboronate group was introduced as a responsive unit, affording the probe TQT-Bpin[33]. In the unactivated state, the quaternary ammonium salt formed between the pinacol phenylboronate and dimethylaniline weakens the electron-donating ability of the donor, thereby suppressing the ICT effect. Reaction with $H_2O_2$ cleaves this moiety, restoring the strong ICT effect and thus triggering a significant NIR-II fluorescence turn-on response.

The synthesis process of TQT-Bpin is displayed in Scheme 2. Intermediate **3** was first synthesized *via* a Stille coupling reaction between 4,7-dibromo-5,6-dinitrobenzo[c][1,2,5]thiadiazole and *N*,*N*-dimethyl-4-(tributylstannyl)aniline. Subsequent reduction of intermediate **3** afforded intermediate **4**, which was then condensed with 1,2-di(thiophen-2-yl)ethane-1,2-dione in a cyclization reaction to yield TQT-DMA. Finally, quaternization of TQT-DMA furnished the target probe, TQT-Bpin. The structure of TQT-Bpin was fully characterized by $^1$H NMR, $^{13}$C NMR, and HRMS(Figs.S1—S7, see the supporting information of this paper).

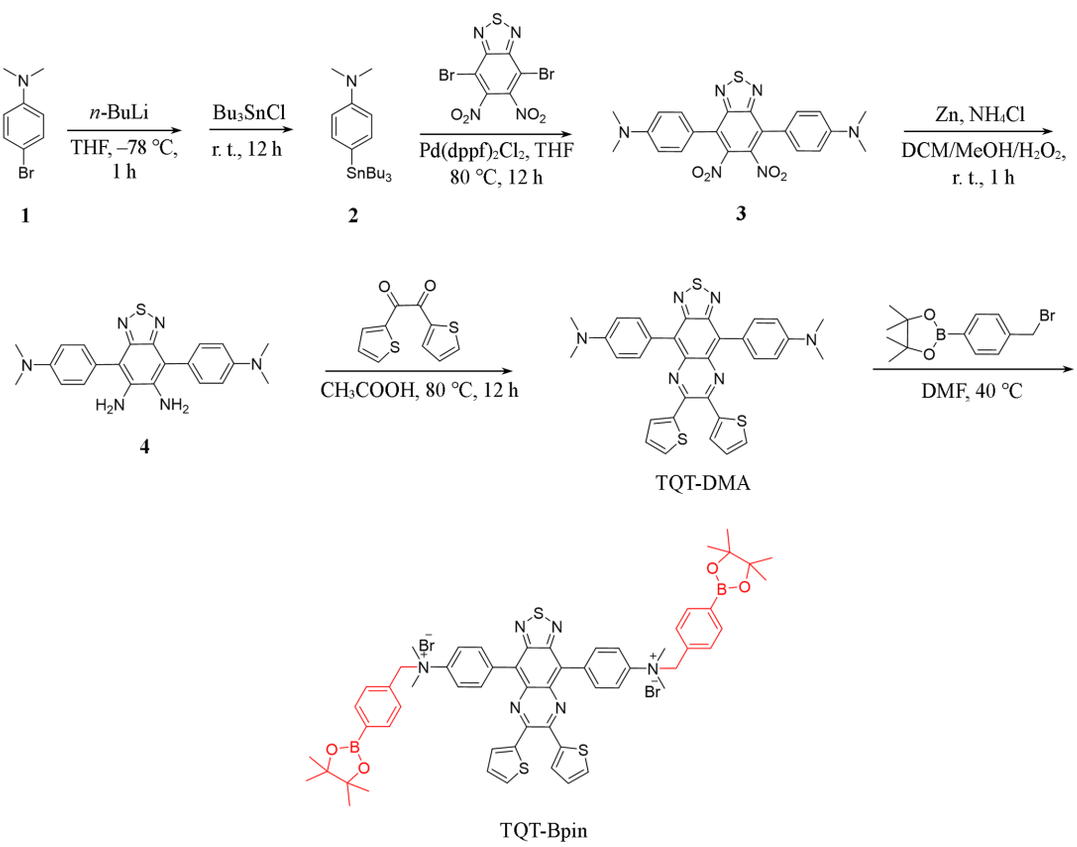


**Scheme 2 Synthetic route of TQT-DMA and TQT-Bpin**

### 3.2 Response Performance to $H_2O_2$

The absorption and emission spectra of the probe TQT-Bpin and the fluorophore TQT-DMA were initially characterized. As described in Figs.1(A) and (B), TQT-DMA displays a markedly red-shifted CT absorption band relative to TQT-Bpin, enabling it to be excited by 808 nm excitation. Notably, TQT-DMA shows a strong NIR-II emission peak at 1004 nm, while TQT-Bpin emits only in the visible region (582 nm) with no significant NIR-II window. The marked difference in their photophysical properties further supports the potential of TQT-Bpin as an activatable NIR-II probe. In addition, TQT-DMA exhibits a large Stokes shift of up to 320 nm, which is beneficial to reduce self-absorption and enhance imaging performance in biological systems.

Based on the predetermined design strategy, the TQT-DMA molecule was designed to form insoluble

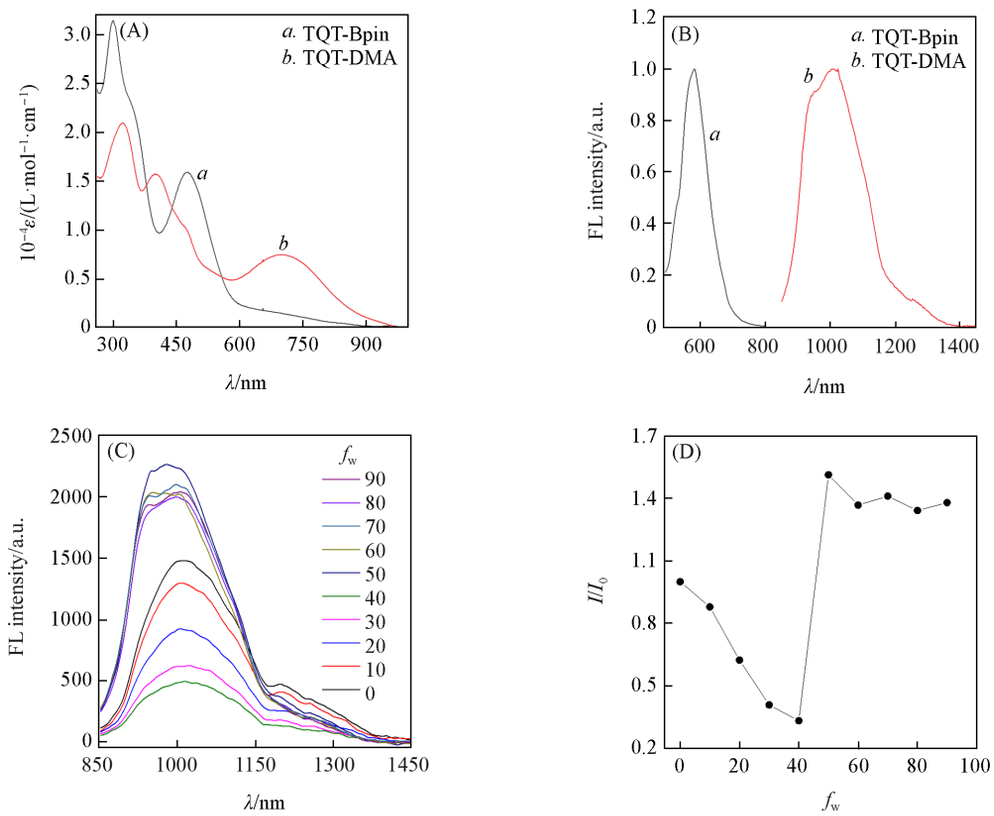


**Fig. 1 Photophysical characterizations of TQT-Bpin and TQT-DMA**

(A, B) Absorption (A) and FL spectra (B) of TQT-Bpin (50 μmol/L) and TQT-DMA (50 μmol/L) in PBS [containing 5% volume fraction DMSO]; (C) FL spectra of TQT-DMA (10 μmol/L) in mixed solvents of DMSO/$H_2O$ with different volume fraction of water ($f_w$); (D) AIE curve of TQT-DMA (10 μmol/L) DMSO/$H_2O$ with increasing water volume fraction, $\lambda_{ex}$=808 nm.

aggregates upon $H_2O_2$ activation, concurrently generating NIR-II emission. Thus, the AIE properties of TQT-DMA were investigated. The Fluorescence (FL) spectra were measured in DMSO/$H_2O$ mixture with increasing the volume fractions of water ($f_w$). As exhibited in Figs. 1 (C) and (D), TQT-DMA in pure DMSO solution displayed faint emission owing to the active molecular motion. When the volume fraction of water was increased from 10% to 40%, the emission intensity gradually decreased while the emission wavelength progressively red-shifted. This phenomenon is attributed to the twisted intramolecular charge transfer (TICT) effect caused by the increased polarity of the mixed solvent[34]. Upon further increasing the water volume fraction, TQT-DMA gradually forms aggregates. The intermolecular interactions effectively suppress molecular motion, thereby suppressing non-radiative decay pathways and leading to a significant enhancement of fluorescence[35]. In addition, we measured the absolute quantum yield of TQT-DMA aggregate in a PBS solution containing 5% (volume fraction) DMSO to be 0.02%. The results confirm that TQT-DMA exhibits typical AIE characteristics and demonstrate its potential for high-contrast fluorescence imaging in physiological environments.

To elucidate the response mechanism of TQT-Bpin toward $H_2O_2$, density functional theory (DFT) calculations were performed to systematically analyze the structural and electronic properties of TQT-Bpin and its reaction product, TQT-DMA. As shown in Fig. 2 (A), owing to the strong electron-withdrawing nature of the acceptor unit, the lowest unoccupied molecular orbital (LUMO) electron density distributions of TQT-Bpin and TQT-DMA are similar, being primarily localized on the [1,2,5]thiadiazolo[3,4-g]quinoxaline moiety. By contrast, distinct differences are observed in the highest occupied molecular orbital (HOMO) electron

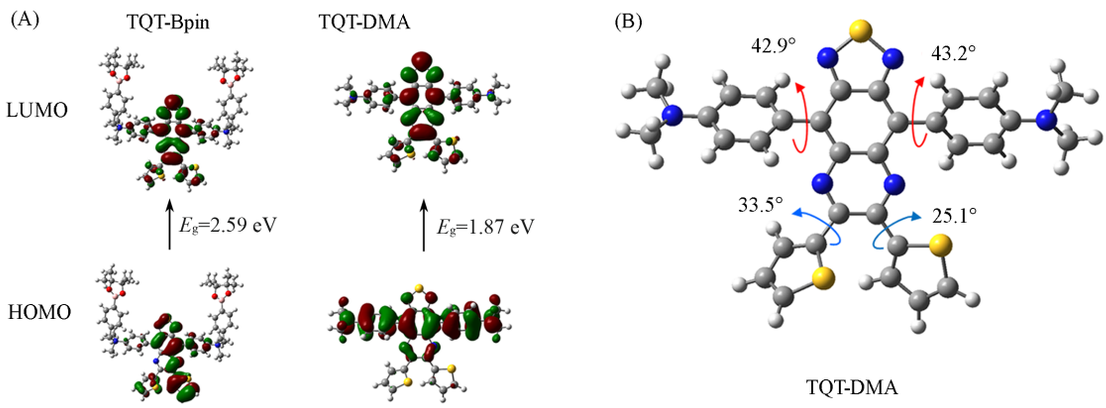


**Fig. 2 DFT calculation of HOMO, LUMO, and the torsion angle of the designed probes**

(A) The frontier orbital electron cloud distribution and energy gaps of TQT-Bpin and TQT-DMA; (B) optimized molecular structure and torsion angles.

density distributions. In TQT-Bpin, the presence of the phenylboronic acid pinacol ester group creates a quaternary ammonium-like structure, which attenuates the electron-donating ability of the dimethylaniline moiety. Consequently, the HOMO is primarily distributed on the acceptor and thiophene moieties, exhibiting substantial spatial overlap with the LUMO. Such significant spatial overlap between the frontier molecular orbitals is detrimental to ICT[36]. In contrast, in TQT-DMA, the HOMO is predominantly localized on the electron-donating dimethylaniline moiety, with partial extension to the benzene ring of the acceptor unit, resulting in a more segregated frontier orbital distribution. This spatial separation facilitates enhanced ICT, leading to a red shift in both absorption and emission wavelengths[18]. Furthermore, geometry optimization reveals that TQT-DMA adopts a twisted spatial conformation[Fig.2(B)], which helps suppress $\pi$-$\pi$ stacking interactions in the aggregated state, thereby enhancing its luminescence efficiency[37].

To determine whether TQT-Bpin could react with $H_2O_2$ and decompose into the TQT-DMA, the absorption spectra were measured. As shown in Figs.3(A)—(D), upon the addition of $H_2O_2$, the absorption peak at 475 nm decreased progressively, while a new peak emerged at 680 nm and intensified significantly over time. Concurrently, the absorption at 808 nm gradually increased, confirming that the product can be efficiently excited at this wavelength. Subsequently, fluorescence spectra were also recorded for the reaction mixture of TQT-Bpin and $H_2O_2$[Figs.3(E) and (F)]. The fluorescence signal of TQT-Bpin at 1004 nm was initially weak. Following the addition of $H_2O_2$, a gradual increase in fluorescence intensity at 1004 nm was observed. The final absorption and emission spectra of the reaction system were nearly identical to those of TQT-DMA, confirming that TQT-Bpin reacts with $H_2O_2$ to release the fluorophore TQT-DMA. For quantitative analysis, $H_2O_2$ solutions with varying concentrations were added to TQT-Bpin solution with a concentration of 50 μmol/L. As the $H_2O_2$ concentration was increased from 0 to 1000 μmol/L, the fluorescence intensity of the solution enhanced approximately 22-fold[Fig.3(G)]. A satisfactory linear relationship ($R^2$=0.9827) between fluorescence intensity at 1004 nm and $H_2O_2$ concentration was observed in the range of 10 to 500 μmol/L. The detection limit was calculated to be 3.6 μmol/L[Fig.3(H)]. Additionally, we utilized DLS to measure the changes in particle size of the probe before and after its response to $H_2O_2$. As shown in Fig.3(I), following the reaction with $H_2O_2$, the particle size of the probe increased from 190 nm to 295 nm, indicating that the responsive group was cleaved off and TQT-Bpin was converted into the more hydrophobic TQT-DMA. These results collectively demonstrate that TQT-Bpin enables the quantitative and highly sensitive detection of $H_2O_2$.

To evaluate its selectivity, TQT-Bpin was incubated with various relevant analytes, including metal ions

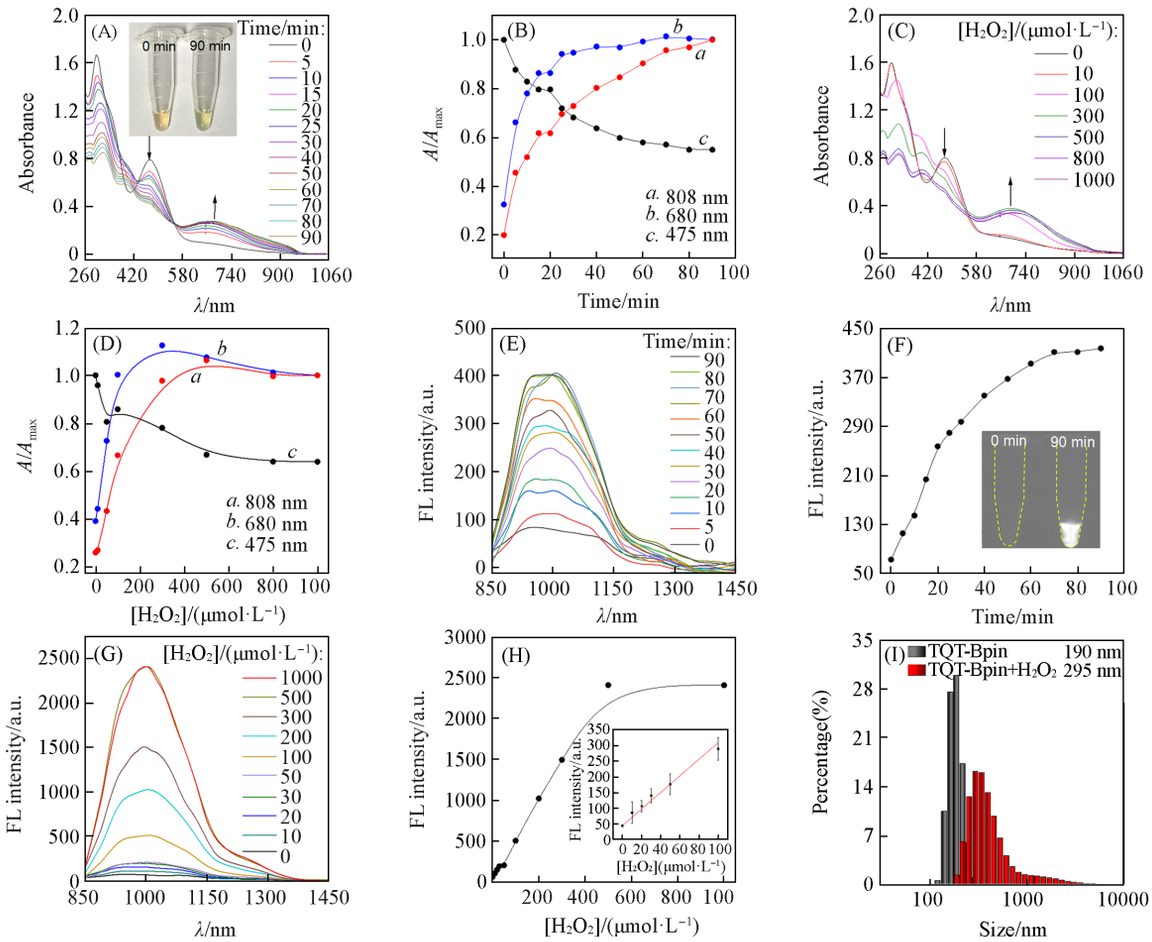


**Fig. 3 Characterization of the response behaviors of TQT-Bpin probe toward $H_2O_2$**

(A) Time-dependent absorption spectra of TQT-Bpin (50 μmol/L) upon response to $H_2O_2$ (100 μmol/L); (B) the corresponding changes in relative absorption intensity at 475, 680, and 808 nm over time; (C) absorption spectra of TQT-Bpin (50 μmol/L) after responding to different concentrations of $H_2O_2$ for 1.5 h; (D) the corresponding relative absorption intensity at 475, 680, and 808 nm plotted against $H_2O_2$ concentration; (E) time-dependent FL spectra of TQT-Bpin (50 μmol/L) upon response to $H_2O_2$ (100 μmol/L); (F) the corresponding changes in FL intensity at 1004 nm over time; (G) FL spectra of TQT-Bpin (50 μmol/L) after responding to different concentrations of $H_2O_2$ for 1.5 h; (H) the corresponding FL intensity at 1004 nm plotted against $H_2O_2$ concentration: the inset shows the linear fit of the fluorescence intensity change at 1004 nm with $H_2O_2$ concentration with fitting equation of $y$=45.23+2.64$x$, in which $y$ means FL intensity, $x$ means $H_2O_2$ concentration, $R^2$=0.9827. $\lambda_{ex}$=808 nm; (I) dynamic light scattering (DLS) characterization of the diameters of TQT-Bpin (50 μmol/L) before and after response to 100 μmol/L $H_2O_2$.

Insets: (A) the solution color change of TQT-Bpin before and after response to $H_2O_2$; (B) the fluorescence change of the solution before and after the response of TQT-Bpin to $H_2O_2$.

($Cu^{2+}$, $Fe^{3+}$), RNS($NO_3^-$, $NO_2^-$), and ROS($ClO^-$, ·OH, $^1O_2$, and TBHP). As shown in Figs.4(A) and (B), a pronounced fluorescence change was observed only in the presence of $H_2O_2$, whereas the influence of other analytes on the fluorescence was negligible. These results imply that TQT-Bpin possesses excellent selectivity for $H_2O_2$ over other potential interferents, thereby enabling its accurate detection of $H_2O_2$ in complex living systems. Subsequently, the chemical stability of TQT-Bpin was evaluated by monitoring its responsiveness in PBS and cell lysate over periods of 24, 48, and 120 h (Figs.S8 and S9, see the supporting information of this paper). Furthermore, the particle size of TQT-Bpin remained stable over a period of 72 h (Fig.S10, see the supporting information of this paper). As shown in Figs.4(C) and (D), the absorption and emission spectra of TQT-Bpin remained unchanged, yet the probe retained strong responsiveness to $H_2O_2$. This confirms that TQT-Bpin exhibits excellent stability across various physiologically relevant environments.

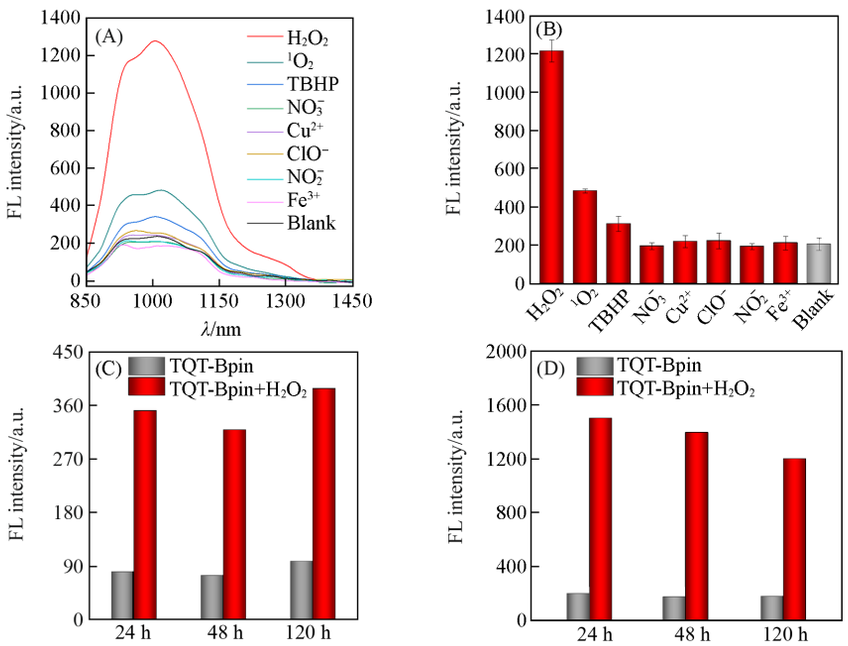


**Fig. 4 Selectivity and stability test of TQT-Bpin**

(A) FL spectra of the molecule after reacting with different analytes (100 μmol/L) for 1.5 h; (B) the corresponding FL intensity at 1004 nm; (C, D) the response of TQT-Bpin to hydrogen peroxide after being stored in PBS (C) and cell lysate (D) for different numbers of hours.

### 3.3 *In situ* Activating Fluorescence in the Tumor

By measuring the viability of cells after incubation with different concentrations of TQT-Bpin, it was demonstrated that the molecule has good biosafety (Fig.S11, see the supporting information of this paper). Given the outstanding fluorescence performance of the probe *in vitro*, we further evaluated its capability for $H_2O_2$ sensing and imaging in biological systems. Since elevated levels of $H_2O_2$ are reported in tumor tissues, we investigated the potential of TQT-Bpin for imaging $H_2O_2$ in CT26 tumor-bearing mice. The bright-field image of the tumor-bearing mice is shown in Fig.S12 (see the supporting information of this paper). Following intratumoral injection of the TQT-Bpin probe solution, the fluorescence intensity in the tumor region gradually increased over time [Fig.5(A)]. In contrast, no fluorescence signal was ever detected in the tumor area of

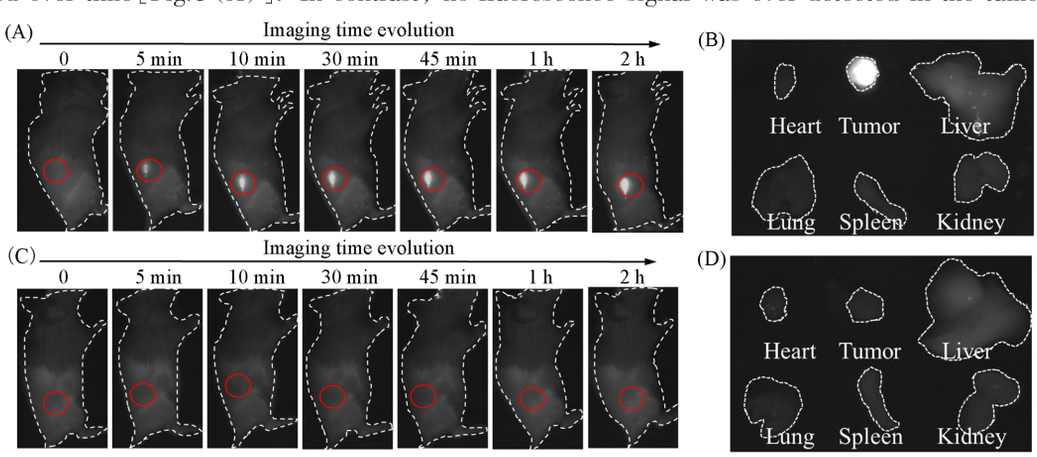


**Fig. 5 Time-dependent imaging in CT26 tumor-bearing mice and imaging of various organs and tumors after dissection after intratumoral injection of TQT-Bpin probe**

(A) Experimental group: *in vivo* imaging of mice over time after intratumoral injection of 100 μL of TQT-Bpin (50 μmol/L); (B) *ex vivo* imaging of organs and tumors from the experimental group at 36 h post-injection; (C) control group: *in vivo* imaging of mice over time after intratumoral injection of 100 μL PBS; (D) *ex vivo* imaging of organs and tumors from the control group at 36 h post-injection.

mice injected with PBS alone[Fig.5(C)]. These results indicate that the probe can be activated *in situ* by the highly expressed $H_2O_2$ in the tumor, enabling highly sensitive NIR-II imaging[38]. At 36 h post-injection, the mice were euthanized and subjected to *ex vivo* organ imaging. Only significant fluorescence signal could be detected in the tumor tissue, and no notable signal in major organs[Figs.5(B) and (D)]. This indicates that TQT-Bpin exhibits favorable tumor retention, supporting its utility for long-term *in situ* monitoring and imaging.

## 4 Conclusions

In this study, we have developed an activatable fluorescent probe capable of specifically responding to intratumoral $H_2O_2$, enabling highly sensitive detection and imaging of hydrogen peroxide in the tumor region. The TQT-Bpin probe, composed of TQT-DMA as a fluorophore and a phenylboronic acid pinacol ester as a recognition group, features NIR-II emission(1004 nm), large Stokes shift(320 nm), high selectivity(LOD=3.6 μmol/L) and good stability. Benefiting from its excellent properties, TQT-Bpin has successfully achieved *in situ* activation and high-sensitivity imaging of tumors in mice. Unlike conventional imaging techniques such as CT, PET, and MRI, which suffer from limited sensitivity, specificity, or radiation risk, the TQT-Bpin probe offers a compelling alternative by combining simple synthesis(requiring only five steps without column chromatography purification), fast probe response(reaching saturation within 90 min), high signal-to-noise ratio(6-fold), good selectivity(capable of distinguishing singlet oxygen, ferric iron, and other oxidizing species). Moreover, the probe also displays good biocompatibility(cell viability>90% even at a concentrations of 100 μmol/L), free of radiotoxicity, and deep tissue penetration stemed from the efficient NIR-II emission. These features effectively overcome the shortcomings of traditional techniques, demonstrating unique potential for early tumor diagnosis. Compared with conventional fluorescent probes, TQT-Bpin possesses longer excitation and emission wavelengths, thereby enabling deeper tissue penetration and a higher signal-to-noise ratio in living systems. This work not only provides a novel strategy for the design of activatable NIR-II probes but also successfully constructs a new fluorescent probe with promising potential for clinical translation.

The supporting information of this paper see http://www.cjcu.jlu.edu.cn/CN/10.7503/cjcu20260058.

### References

[1] Xu C., Qin X., Wei X., Yu J., Zhang Y., Zhang Y., Ding D., Song J., Pu K., *Nat. Nanotechnol.*, **2024**, *20*, 286—295
[2] Xu Z., Lv M., Yang J., Li T., Lv J., Li J., Xiao H., Yang Y., Zhou S., Tan X., Cheng L., Guo H., Xi L., Shao P. L., Zhang B., *Aggregate*, **2025**, *6*, e70040
[3] Hu Y., Gao X., Ma J., Shangguan Z., Chen L., Zhang G., Zhang X. S., Li C., Li Y., Zhang D., *Aggregate*, **2025**, *6*, e735
[4] Chen Y., Wang S., Zhang F., *Nat. Rev. Bioeng.*, **2023**, *1*, 60—78
[5] Xiong L. H., He X., Zhao Z., Kwok R. T. K., Xiong Y., Gao P. F., Yang F., Huang Y., Sung H. H. Y., Williams I. D., Lam J. W. Y., Cheng J., Zhang R., Tang B. Z., *ACS Nano*, **2018**, *12*, 9549—9557
[6] Sun J., Xiong L. H., Tang B. Z., He X., *Natl. Sci. Rev.*, **2026**, *13*, nwaf424
[7] Hanaoka K., Iwaki S., Yagi K., Myochin T., Ikeno T., Ohno H., Sasaki E., Komatsu T., Ueno T., Uchigashima M., Mikuni T., Tainaka K., Tahara S., Takeuchi S., Tahara T., Uchiyama M., Nagano T., Urano Y., *J. Am. Chem. Soc.*, **2022**, *144*, 19778—19790
[8] Chen L., Peng M., Ouyang Y., Chen J., Li H., Wu M., Qu R., Zhou W., Zhang C., Jiang Y., Xu S., Wu W., Jiang X., Zhen X., *J. Am. Chem. Soc.*, **2025**, *147*, 17330—17341
[9] Sun J., Geng J., Tang B. Z., He X., *Adv. Funct. Mater.*, **2024**, *34*, 2315299
[10] Zhang Y., Sun J., Xiong L. H., Tang B. Z., He X., *Adv. Funct. Mater.*, **2025**, *35*, 2509090
[11] Lam K. W. K., Chau J. H. C., Yu E. Y., Sun F., Lam J. W. Y., Ding D., Kwok R. T. K., Sun J., He X., Tang B. Z., *ACS Nano*, **2023**, *17*, 7145—7156
[12] He X., Zeng T., Li Z., Wang G., Ma N., *Angew. Chem. Int. Ed.*, **2016**, *55*, 3073—3076
[13] Li Y., Liu G., Cheng S., Zhang J., Yao X., Xie X., Xu C., Tang Y., Wang X., Tang B., *Chem. Rev.*, **2025**, *125*, 7725—7810

[14] Zhou Y., Yang X., Lee H., Yan M., Yoon J., *Coord. Chem. Rev.*, **2025**, *541*, 216785
[15] Wang W. X., Jiang W. L., Mao G. J., Tan M., Fei J., Li Y., Li C. Y., *Anal. Chem.*, **2021**, *93*, 3301—3307
[16] Xie Z., Huang J., Zeng W., Li X., Cheng D., Zhou J., He L., *Sens. Actuators B Chem.*, **2026**, *447*, 138814
[17] Jiang R., Cai Z., Bai H., Liu Y., Zu B., Dou X., *Anal. Chem.*, **2025**, *97*, 11669—11677
[18] Ma F., Zhang R., Wang B., Liang Z., Zhang S., Jiang J., Tan H., Xing G., Kwok R. T. K., Lam J. W. Y., Zhao Z., Tang B. Z., *J. Am. Chem. Soc.*, **2025**, *147*, 29815—29828
[19] Li J., Dong Y., Wei R., Jiang G., Yao C., Lv M., Wu Y., Gardner S. H., Zhang F., Lucero M. Y., Huang J., Chen H., Ge G., Chan J., Chen J., Sun H., Luo X., Qian X., Yang Y., *J. Am. Chem. Soc.*, **2022**, *144*, 14351—14362
[20] Shen H., Sun F., Zhu X., Zhang J., Ou X., Zhang J., Xu C., Sung H. H. Y., Williams I. D., Chen S., Kwok R. T. K., Lam J. W. Y., Sun J., Zhang F., Tang B. Z., *J. Am. Chem. Soc.*, **2022**, *144*, 15391—15402
[21] Song Y., Tong X., Han Y., Zhang Q. W., *Aggregate*, **2024**, *6*, e680
[22] Ma F., Zhang S., Jiang J., Liu Y., Sun J., Lam J. W. Y., Zhao Z., Tang B. Z., *Adv. Mater.*, **2025**, *37*, e2414188
[23] Hong Y., Lam J. W., Tang B. Z., *Chem. Commun.*, **2009**, *29*, 4332—4353
[24] Mei J., Leung N. L., Kwok R. T., Lam J. W., Tang B. Z., *Chem. Rev.*, **2015**, *115*, 11718—11940
[25] Lam K. W. K., Zhang Y., Du W., Sun J., Sun F., Chen Y., Ma C. C. H., Lam J. W. Y., Kwok R. T. K., Sun J., He X., Tang B. Z., *ACS Nano*, **2025**, *19*, 24701—24712
[26] Mei J., Hong Y., Lam J. W., Qin A., Tang Y., Tang B. Z., *Adv. Mater.*, **2014**, *26*, 5429—5479
[27] Chen P. Y., Zhang G. Y., Li J. G., Ma L. J., Zhao J. Y., Zhu M. G., Li S., Wang Z., *Chem. Res. Chinese Universities*, **2024**, *40*(2), 293—304
[28] Xiong J. Y., Wu M. J., Yao L. Y., *Chem. Res. Chinese Universities*, **2024**, *40*(5), 887—893
[29] Sun Z. H., Yin P. P., He S. Y., Zhang K. G., Pan X. R., Wang J. Y., Hao P. N., Zhou Z., Yang X. G., Ma L. F., Tan C. L., *Chem. Res. Chinese Universities*, **2025**, *41*(3), 519—524
[30] Hong Y. N., Lam J. W. Y., Tang B. Z., *Chem. Soc. Rev.*, **2011**, *40*, 5361—5388
[31] Xiong L. H., Yang L., Geng J., Tang B. Z., He X., *ACS Nano*, **2024**, *18*, 17837—17851
[32] Ji A., Lou H., Qu C., Lu W., Hao Y., Li J., Wu Y., Chang T., Chen H., Cheng Z., *Nat. Commun.*, **2022**, *13*, 3815
[33] Cabello M. C., Chen G., Melville M. J., Osman R., Kumar G. D., Domaille D. W., Lippert A. R., *Chem. Rev.*, **2024**, *124*, 9225—9375
[34] Wu H., Fan X. C., Wang H., Huang F., Xiong X., Shi Y. Z., Wang K., Yu J., Zhang X. H., *Aggregate*, **2022**, *4*, e243
[35] Chen X., Zhang S., Jiang Y., He G., Zhang M., Wang J., Deng Z., Wang H., Lam J. W. Y., Hu L., Tang B. Z., *Angew. Chem. Int. Ed.*, **2024**, *63*, e202402175
[36] Zhang W., Kong J., Miao R., Song H., Ma Y., Zhou M., Fang Y., *Adv. Funct. Mater.*, **2023**, *34*, 2311404
[37] Huo Y., Qi H., He S., Li J., Song S., Lv J., Liu Y., Peng L., Ying S., Yan S., *Aggregate*, **2023**, *4*, e391
[38] Dou K., Lu J., Xing Y., Wang R., Won M., Kim J., Yu F., Kim J. S., *Angew. Chem. Int. Ed.*, **2025**, *64*, e202419191

(Ed.: W, K, M)